Nano Research
2022, 15(7): 6121–6127

ISSN 1998-0124 CN 11-5974/O4
https://doi.org/10.1007/s12274-022-4195-8

Research Article

Perovskite bridging PbS quantum dot/polymer interface enables efficient solar cells

Xing Meng[1,§], Yifan Chen[1,§], Fan Yang[1], Jieqi Zhang[3], Guozheng Shi[1], Yannan Zhang[1], Haodong Tang[4], Wei Chen[4], Yang Liu[1], Lin Yuan[1], Shaojuan Li[2], Kai Wang[4], Qi Chen[3], Zeke Liu[1,2] (✉), and Wanli Ma[1] (✉)

[1] *Institute of Functional Nano & Soft Materials (FUNSOM), Soochow University, Suzhou 215123, China*
[2] *State Key Laboratory of Applied Optics, Changchun Institute of Optics Fine Mechanics and Physics, Changchun 130033, China*
[3] *i-Lab, CAS Center for Excellence in Nanoscience, Suzhou Institute of Nano-Tech and Nano-Bionics, Suzhou 215123, China*
[4] *Department of Electrical and Electronic Engineering, Southern University of Science and Technology, Shenzhen 518055, China*
[§] *Xing Meng and Yifan Chen contributed equally to this work.*

Received: 19 December 2021 / **Revised:** 17 January 2022 / **Accepted:** 24 January 2022

ABSTRACT

Conjugated polymers have been explored as promising hole-transporting layer (HTL) in lead sulfide (PbS) quantum dot (QD) solar cells. The fine regulation of the inorganic/organic interface is pivotal to realize high device performance. In this work, we propose using $CsPbI_3$ QDs as the interfacial layer between PbS QD active layer and organic polymer HTL. The relative soft perovskite can mediate the interface and form favorable energy level alignment, improving charge extraction and reducing interfacial charge recombination. As a result, the photovoltaic performance can be efficiently improved from 10.50% to 12.32%. This work may provide new guidelines to the device structural design of QD optoelectronics by integrating different solution-processed semiconductors.

KEYWORDS

lead sulfide quantum dot, solar cells, perovskite, energy level alignment

1 Introduction

Solution-processed lead sulfide (PbS) quantum dot (QD) solar cells have received tremendous attention because their optical and electronic properties can be conveniently tuned due to the quantum confinement effect and the large surface-to-volume ratio of QDs [1, 2]. Meanwhile, the solution processability of QDs endows them as ideal building blocks to fabricate low-cost, large-area, and flexible optoelectronic devices [3–5].

The study of surface chemistry and the development in device engineering have boosted the power conversion efficiency (PCE) of PbS QD solar cells from < 1% to 14% in the past two decades [6–18]. An ideal QD solar cell structure pursues interfacial layers that host advances in charge extraction with minimized energetic losses. These request high charge carrier mobility, low-trap state density, and well-matched energetic alignment with preferable interfacial contact in the buffer layer, which makes the optimization of hole transport layers well-concerned in the studies of CQD solar cells [19–22]. In 2014, Bawendi and coworkers first reported an efficient and stable device structure with iodine-capped PbS QDs as the active layer and ethanedithiol (EDT)-capped PbS as the p-type hole-transporting layer (HTL), which was then widely applied in the following years [11, 23–27]. However, the EDT-PbS has to be deposited through the complicated layer-by-layer (LBL) method based on the solid-state ligand exchange process, which is incompatible with commercial high-throughput deposition manufacturing. Meanwhile, this process may introduce trap states, limiting device performance [28, 29]. Thereafter, p-type organic semiconductors processed by single-layer deposition have been adopted as the HTL in PbS QD solar cells, whose optoelectronic properties can be flexibly tuned by manipulating their chemical structures [30]. Several strategies have been applied to improve hole extraction by using organic HTLs, including the exploration of new organic materials [31–33], organic heterojunctions [34, 35], and the patterning of organic HTLs [18, 36]. The highest PCE of the PbS QD solar cells with organic HTL has reached 13.3%, which was further improved to 14% by employing a scattering layer [18]. On the other hand, the interface between the inorganic QDs and organic polymers is still unsatisfactory according to the extensive experience in the field of polymer/QDs hybrid solar cells [37, 38]. This may hinder device charge transport and extraction, and should be addressed to further improve the device performance of QD solar cells based on polymer HTLs.

Apart from PbS QDs, lead halide perovskite QDs have also become emerging photovoltaic materials due to their superior optoelectronic properties and high defect tolerance [39–43]. The energy level alignment between the PbS/perovskite QD interface can be adjusted and matched by manipulating the size, surface ligand, or composition of both QDs [44]. Additionally, the softness of perovskite materials is just between PbS and organic polymer, which makes them desired candidates to modulate the PbS QD/polymer interface [45, 46]. Therefore, it is worth exploring the novel device structure by integrating both two QD

Address correspondence to Zeke Liu, zkliu@suda.edu.cn; Wanli Ma, wlma@suda.edu.cn

materials. However, this promising direction has never been seriously explored.

In this work, we demonstrate a new strategy to improve hole extraction by introducing $CsPbI_3$ QDs as the interfacial layer between the PbS QD active layer and poly[(ethylhexyl-thiophenyl)-benzodithiophene-(ethylhexyl)-thienothiophene] (PTB7-Th) HTL. The insertion of the $CsPbI_3$ QD interfacial layer can form graded energy levels, improving hole extraction and reducing charge recombination. In addition, this interfacial layer can build a dipole-charge distribution at the $CsPbI_3$ QD/PbS QD interface, improving charge collection. As a result, the PCE can be significantly improved from 10.50% (control device) to 12.32%. The results indicate that the combinative use of different QD materials can provide a new path to further improve the interface and device performance of QD solar cells.

2 Results and discussion

As illustrated in Fig. 1(a), long aliphatic ligand-capped PbS and $CsPbI_3$ QDs with cubic crystal structures were synthesized according to previous reports [47, 48]. The corresponding transmission electron microscopy (TEM) images, absorbance spectra, and photoluminescence (PL) spectra are shown in Fig. 1(b) and Fig. S1 in the Electronic Supplementary Material (ESM). The schematic architecture and the cross-sectional scanning electron microscopy (SEM) image of the QD solar cells used in this study are shown in Figs. 1(b) and 1(c). The PbS QD films prepared from the solution-phased ligand exchanged inks serve as the light absorbers. The $CsPbI_3$ dispersed in octane can be well deposited on top of PbS CQDs without introducing any surface damage. After deposition, the $CsPbI_3$ QD film was treated with methyl acetate (MeOAc) to partially remove surface ligands for improved conductivity. Then an organic PTB7-Th layer was subsequently deposited as the HTL. The polymer chemical structure is shown in Fig. 1(a) and the absorbance spectrum is shown in Fig. S2 in the ESM. Therefore, the $CsPbI_3$ QDs serve as an interfacial layer between the PbS QDs and HTL (Fig. 1(d)).

Ultraviolet photoelectron spectroscopy (UPS) was first applied to measure the energy levels of each functional layer (Fig. S3 in the ESM). The band alignment for the PbS CQD devices is depicted in Figs. 2(a) and 2(b). Both the valence band (VB) and conduction band (CB) of the $CsPbI_3$ QD layer were located between those of PbS QD and PTB7-Th layers. This band alignment creates a graded pathway for charge extraction and may facilitate hole

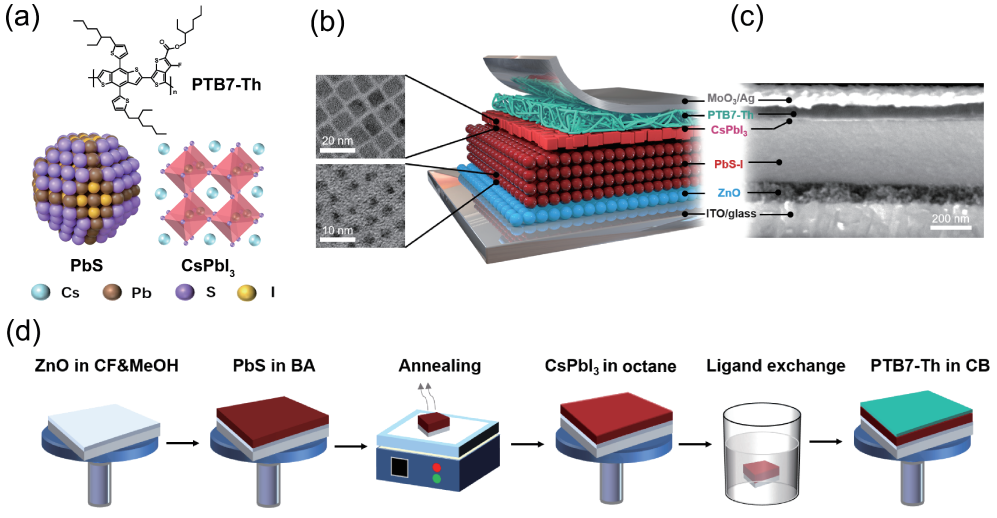

Figure 1 (a) Molecular structure of PTB7-Th and illustration of I-capped PbS CQD and $CsPbI_3$ QDs. (b) Schematic diagram of the QD photovoltaic device used in this study. (c) Cross-sectional SEM image of the same device. (d) Schematic diagram of film-fabrication.

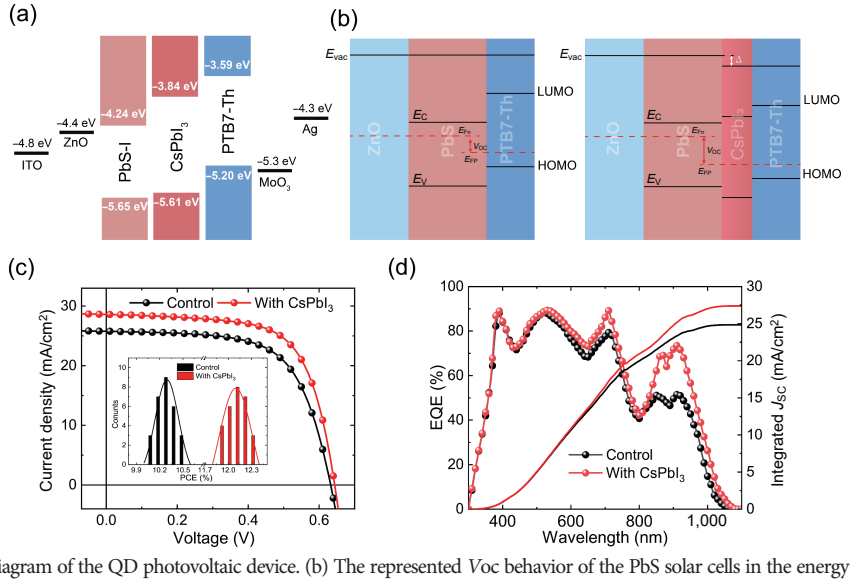

Figure 2 (a) Energy levels diagram of the QD photovoltaic device. (b) The represented *Voc* behavior of the PbS solar cells in the energy level diagrams. (c) *J*–*V* curve of the optimized QD photovoltaic device with and without (control) the $CsPbI_3$ QDs interlayer. And the inset shows reproducibility of the 28 independent devices. (d) EQE of the optimized QD photovoltaic device with and without (control) the $CsPbI_3$ QDs interlayer.

transfer, leading to reduced interfacial charge recombination. In comparison, charge accumulation may occur at the PbS CQD/polymer interface in the control devices. We first optimized the thickness of the $CsPbI_3$ QD layer for solar cells. It was shown that the $CsPbI_3$ QD layer coated from the solution with a concentration of 10 mg/mL gave the best performance (Fig. S4 in the ESM). We also optimized the thickness of the organic HTL. The optimal thickness of PTB7-Th layer is determined to be around 25 nm (corresponding to a concentration of 5 mg/mL for the cast solution (Fig. S5 in the ESM)). The top-view SEM image clearly visualizes a distinct layer of $CsPbI_3$ QDs deposited on the PbS QD layer and the presence of $CsPbI_3$ QD has no significant effect on the morphology of above PTB7-Th (Fig. S6 in the ESM). It has been reported that surface ligand removal and passivation have a huge effect on the optoelectronic properties of $CsPbI_3$ QDs [49]. Thus, we further optimized the surface treatment process by using guanidinium thiocyanate (GASCN) (Table S1 in the ESM, a detailed description is presented in the Experimental section) [50]. In short, the introduction of a graded energy level in PbS CQD solar cells demonstrates a significant improvement in device performance. The current–voltage (J–V) characteristics of the optimized device together with the control device under simulated AM 1.5G illumination are shown in Fig. 2(c). The average and the best device photovoltaic parameters are summarized in Table 1. The control device presents a decent PCE of 10.50% with an open-circuit voltage (V_{oc}) of 0.63 V, a short-circuit current density (J_{sc}) of 25.77 mA/cm^2, and a fill factor (FF) of 64.7%, which is close to the photovoltaic performance in previous reports with the same device structure [33, 35]. The champion device with the $CsPbI_3$ QD interfacial layer exhibits a V_{oc} of 0.65 V, a J_{sc} of 28.62 mA/cm^2, and an FF of 66.2%, leading to a significantly enhanced PCE of 12.32%. Accordingly, the devices with the interfacial layer exhibit distinctly higher external quantum efficiency (EQE) values than the control devices (Fig. 2(d)), which agrees well with the improved charge carrier extraction and the enhancement of J_{sc}. The results show that the integrated J_{sc} from the EQE curve and the obtained current densities from the solar simulator are consistent with a mismatch of < 5%. To ensure the reproducibility of the results, 28 independent devices using different batches of QD materials were fabricated and tested. Histograms of the device performance characteristics are shown in the inset of Fig. 2(c). All devices with the $CsPbI_3$ QD interfacial layer show superior performance compared to the control devices.

To explore the origin of the improvement in device performance, optical characterizations were conducted. As shown in Fig. 3(a), the absorptance spectra indicate that the insertion of the thin $CsPbI_3$ QD interfacial layer does not introduce noticeable light absorption. The function of the $CsPbI_3$ QD interfacial layer was further studied using PL spectra. As shown in Fig. 3(b), the PbS/PTB7-Th stack exhibits PL quenching compared to the sole PbS layer, indicating charge transfer between the active layer and organic HTL. After inserting the $CsPbI_3$ QD interfacial layer (PbS/$CsPbI_3$/PTB7-Th), the PL intensity further decreases compared to that of the PbS/PTB7-Th structure, indicating more efficient charge transfer due to the graded band alignment (Fig. 2(a)). In addition, the PbS film exhibits an average PL lifetime of 18.99 ns, which decreases to 3.15 ns for the PbS/PTB7-Th film and 1.58 ns for the PbS/$CsPbI_3$/PTB7-Th film (Fig. 3(c)), further

Table 1 Device performance of solar cells using $CsPbI_3$ QDs as the interfacial layer

Condition		V_{OC} (V)	J_{SC} (mA/cm^2)	FF (%)	PCE (%)
Control	Champion	0.63	25.77	64.70	10.50
	Average[a]	0.62 ± 0.01	25.83 ± 0.86	64.28 ± 0.97	10.28 ± 0.22
$CsPbI_3$	Champion	0.65	28.62	66.21	12.32
	Average[a]	0.65 ± 0.01	28.37 ± 1.01	65.62 ± 1.66	12.14 ± 0.18

[a]Average results based on 28 devices on each condition.

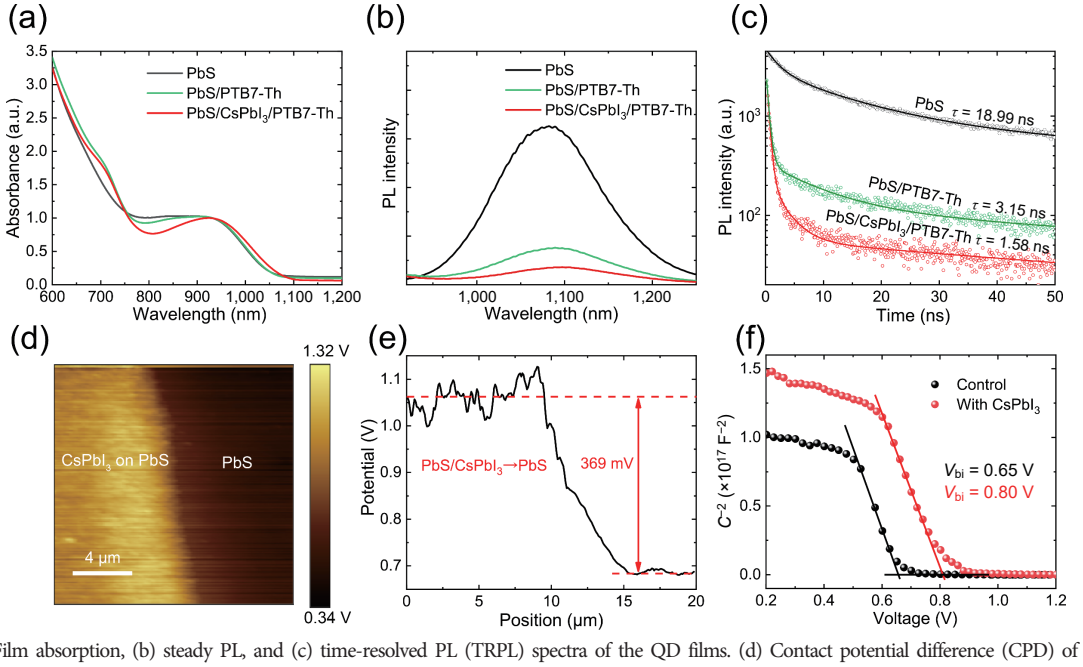

Figure 3 (a) Film absorption, (b) steady PL, and (c) time-resolved PL (TRPL) spectra of the QD films. (d) Contact potential difference (CPD) of the PbS layer partially covered by the $CsPbI_3$ QDs layer. (e) Cross-sectional line profiles of the CPD images in (d). (f) Mott–Schottky plots of the PbS QD devices with and without (control) the $CsPb_3$ QDs interlayer.

confirming the enhanced charge transfer after inserting the $CsPbI_3$ QD interfacial layer. The hole mobility of the HTL layers was measured by the space charge limited current (SCLC) method based on hole-only devices (ITO/PEDOT:PSS/PbS/($CsPbI_3$)/PTB7-Th/MoO_x/Ag) (Fig. S7 in the ESM). As calculated from the logarithm of the J–V curve obtained in the dark condition according to the mobility formula $J = \frac{9}{8}\varepsilon_0\varepsilon_r\mu_{h,e}\frac{V^2}{d^3}$, the hole mobility of the PbS/$CsPbI_3$ QD film is 1.01×10^{-4} $cm^2/V{\cdot}s$, which doubles that of the control film (5.60×10^{-5} $cm^2/V{\cdot}s$). The improved hole transfer and mobility indicate that the insertion of an extra $CsPbI_3$ layer does not hinder hole transport, but enhances hole extraction in QD solar cells instead [32].

To explore the origin of V_{oc} improvement, Kelvin probe force microscopy (KPFM) was employed to measure the contact potential difference (CPD) of the $CsPbI_3$ QD interfacial layer on the PbS QD layer. The CPD = $V_{tip} - V_{sample}$, where V_{tip} and V_{sample} are the potentials of the tip and sample surface, respectively. Therefore, the relative CPDs correspond to the vacuum level shifts of the sample with different surfaces. The CPD image of the interface is shown in Fig. 3(d). The corresponding cross-sectional line profile of the CPD image is shown in Fig. 3(e). A CPD difference up to 369 meV can be extracted for the $CsPbI_3$ QD/PbS QD interface. The work functions for the $CsPbI_3$ QD and PbS QD layers are 4.65 and 4.41 eV (Fig. S3 in the ESM), respectively. The difference of 240 meV between the work function of $CsPbI_3$ QD and PbS QD layers is less than the 369 meV vacuum shift in the KPFM results. This discrepancy indicates that a dipole-charge distribution at the $CsPbI_3$ QD/PbS QD interface may be formed, which reinforces the electric field in solar cells and facilitates hole extraction [51]. The improvement of build-in potentials (V_{bi}) in $CsPbI_3$-inserted solar cells can be confirmed by capacitance–voltage (C–V) measurements [52]. As shown in the Mott–Schottky curves (Fig. 3(f)), V_{bi} was obtained from the $1/C^2 = 0$ intercept. The extracted V_{bi} value of the control devices is 0.65 V, which is seriously lower than that of the device with the $CsPbI_3$ QD interfacial layer (0.80 V). The large V_{bi} introduced by the insertion of the $CsPbI_3$ QD interfacial layer can improve the drift of charge carriers in the depletion region of solar cells and promote charge extraction, which is also responsible for the improved V_{oc} in solar cells [35].

We then carried out several device characterizations to investigate the charge carrier extraction and recombination processes in the devices. As shown in the dark J–V curves (Fig. 4(a)), the leakage current is substantially suppressed after inserting the $CsPbI_3$ QD interfacial layer, while the two devices exhibit similar output currents in the forward direction, indicating a higher rectification ratio and thus improved hole selectivity of the anode after using the $CsPbI_3$ QD interfacial layer [27, 51]. Electrochemical impedance spectroscopy (EIS) was then utilized to study the charge-transfer resistance (R_{tr}) and series resistance (R_s) in the devices. The Nyquist plots of the device with and without the $CsPbI_3$ QD interfacial layer are shown in Fig. 4(b) and Table S2 in the ESM. The obtained R_s and R_{tr} values of the devices with the $CsPbI_3$ QD interfacial layer are 12.54 and 33.15 Ω, respectively. Both values are lower than those of the control device with R_s of 36.68 Ω and R_{tr} of 55.42 Ω, indicating a higher efficiency of interfacial charge transfer after inserting the $CsPbI_3$ QD interfacial layer [35]. The free carrier recombination kinetics were further investigated by using transient photovoltage (TPV) spectroscopy under open-circuit conditions. As shown in Fig. 4(c), the decay curves are fitted and the decay times are calculated to be 555.7 and 204.2 μs for the devices with and without $CsPbI_3$ QD interfacial layer, respectively, which suggests a decrease of charge-carrier recombination after introducing the $CsPbI_3$ QD interfacial layer. Meanwhile, the ideal factor of solar cells was investigated by the dependence of V_{oc} on the light intensity [33]. As shown in Fig. 4(d), the ideal factor can be described as the slope in the V_{oc} plots. For the device with $CsPbI_3$ QD interfacial layer, an ideal factor of 1.49 was found, which is lower than that in the control device (1.54), suggesting reduced charge recombination in the device with the $CsPbI_3$ QD interfacial layer [53].

3 Conclusions

In this study, we report a new strategy to improve the hole extraction of organic HTLs in PbS QD solar cells by introducing $CsPbI_3$ QDs as an interfacial layer. The appropriate energy level of $CsPbI_3$ QDs falls between the active PbS QDs and the organic

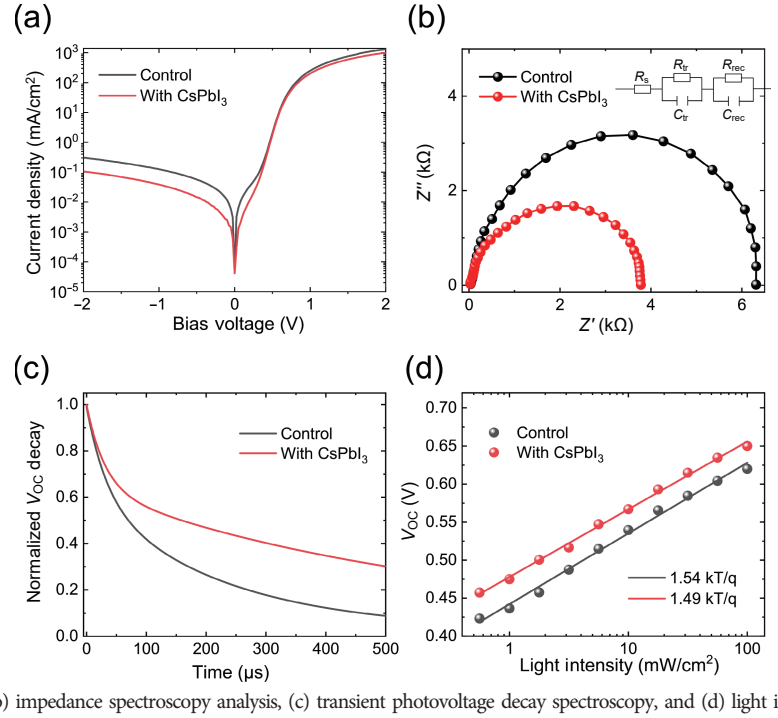

Figure 4 (a) Dark J–V curve, (b) impedance spectroscopy analysis, (c) transient photovoltage decay spectroscopy, and (d) light intensity dependence of V_{oc} of the devices based on QD photovoltaic device with and without $CsPbI_3$ QDs interlayer.

PTB7-Th layer. The formed graded band alignment can promote hole extraction and reduce interfacial charge recombination. Meanwhile, the interfacial layer also produces a dipole-charge distribution at the $CsPbI_3$ QD/PbS QD interface, which improves charge collection and enhances V_{oc}. As a result, the PCE can be efficiently improved from 10.50% to 12.32%. Our results highlight the importance of interfacial manipulation in QD solar cells and proposes a new direction to design advanced device architectures by the combinative use of two typical solution-processed QD photovoltaic materials.

4 Experimental section

4.1 Material preparation

Synthesis of ZnO nanoparticles: ZnO nanoparticles were synthesized according to the following procedures: Zinc acetate dehydrate (2.95 g, 13.4 mmol) was dissolved in methanol (125 mL) with stirring at 63.5 °C. A solution of KOH (1.48 g, 23 mmol) in methanol (65 mL) was then dropwise added over a period of 15 min. The mixed solution was continuously stirred for 3 h. After cooling to room temperature, the solution was then centrifuged and washed with methanol twice. Methanol (10 mL) and chloroform (10 mL) were added to disperse the precipitate.

Synthesis of PbS colloidal quantum dots: 10 mmol of lead acetate trihydrate was dissolved in 7 g of oleic acid and 60 g of 1-octadecene in a three-neck flask by heating the mixture to 100 °C under vacuum for 2 h and then cooled down to 75 °C under nitrogen. 1 mL of hexamethyldisilathiane in 9 mL of 1-octadecene was rapidly injected into the lead precursor solution. After synthesis, the solution was transferred into a nitrogen-filled glovebox. QDs were purified by precipitation in hexane/isopropyl alcohol and stored in solid form in a glovebox.

Ligand exchange and film fabrication: The solution-phase ligand-exchange process was carried out in air. Lead iodide (0.1 M) and NH_4Ac (0.04 M) are predissolved in dimethylformamide (DMF). A 100 mL amount of QD hexane solution (10 mg/mL) was added to 100 mL of the precursor solution. These were mixed vigorously for 2–3 min until the QDs were completely transferred to the DMF phase. The DMF phase was washed five times with hexane. After ligand exchange, QDs were precipitated via the addition of toluene and separated by centrifugation. After 1 h of drying, the QDs were then redispersed in butylamine (350 mg/mL) to facilitate film deposition. The exchanged ink was deposited by single-step spin-coating at 2,500 rpm for 40 s to achieve ~ 350 nm thickness.

Synthesis of $CsPbI_3$ perovskite quantum dots: 1 g of lead iodide and 5 mL oleic acid mixed with 5 mL oleylamine were dissolved in 50 mL of 1-octadecene in a three-neck flask by heating the mixture to 90 °C under vacuum for 1 h to obtain the Pb precursor. 1 g of Cs_2CO_3, 4 mL of OA, and 100 mL of 1-octadecene (ODE) were put into another 250 mL three-necked flask and were stirred and vacuumed at 90 °C for 1 h. Then, N_2 was pumped into the three-necked flask and the reaction temperature increased to 120 °C. Finally, the reaction continued for 50 min to obtain Cs-oleate. 8 mL Cs-oleate was rapidly injected into the Pb precursor solution at 160 °C. After synthesis, the solution was transferred into a nitrogen-filled glovebox. QDs were purified by precipitation with MeOAc and dissolved in hexane and stored in a refrigerator. The $CsPbI_3$ PQD solid was dispersed into octane at 10 mg/mL to prepare a $CsPbI_3$ PQD buffer layer.

4.2 Device fabrication

Fabrication and characterization of PbS QD solar cells: Patterned ITO anodes were sequentially cleaned by deionized water, isopropanol, and acetone in an ultrasonic apparatus, and a following Ultraviolet-ozone treatment for 15 min. ZnO nanoparticles were deposited at 2,500 rpm for 20 s on an ITO substrate under ambient conditions. The PbS QDs were deposited at 2,500 rpm for 40 s onto a ZnO substrate using the exchanged ink and dried at 90 °C for 1 min under ambient conditions with humidity lower than 10%. Then, 15 μL of the as-prepared octane solution of $CsPbI_3$ PQDs was spin-coated on the PbS QD substrate at 1,000 rpm for 15 s and 2,000 rpm for 20 s. Then, 150 μL of methyl acetate (MeOAc) was dropped on the $CsPbI_3$ PQD layer for 5 s to remove the long-chain insulated ligands at the surface of $CsPbI_3$ PQD and spun at 2000 rpm for 20 s. The film was soaked in a saturated solution of ethyl acetate of guanidinium thiocyanate (GASCN) and pure MeOAc for 3 s, and then blown dry. Then, the substrates were transferred into a N_2-filled glovebox, and PTB7-Th (5 mg/mL in chlorobenzene) was spin-coated (2,000 rpm for 40 s) onto the PbS or $CsPbI_3$ QD layer. Finally, silver (Ag) (120 nm) as the cathode was deposited on MoO_3 (8 nm) in a vacuum thermal evaporator. The area of each device was 7.25 mm^2, which was defined through a shadow mask. The performance of all cells was tested under AM 1.5G illumination (Newport, Class AAA solar simulator, 94023A-U). The EQE was determined using certified IPCE equipment (Zolix Instruments, Inc, SolarCellScan100).

4.3 Measurements and characterization

The current density–voltage characteristics of the photovoltaic cells were measured using a Keithley 2400 (*I–V*) digital source meter under simulated AM 1.5 G solar irradiation at 100 mW/cm^2 (Newport, Class AAA solar simulator, 94023A-U). The light intensity was calibrated using a certified Oriel Reference Cell (91 150 V) and verified with an NREL calibrated Hamamatsu S1787-04 diode. Kelvin probe force microscopy (KPFM) measurements were performed under nitrogen conditions with a Bruker Dimension Icon atomic force microscope. (The PbS QD was deposited onto patterned ITO substrate. Then, 5 μL octane solution of $CsPbI_3$ PQDs was spin-coated from the corner of the PbS QDs substrate. MeOAc was dropped on the $CsPbI_3$ PQD layer to remove the long-chain ligands at the surface of $CsPbI_3$ PQD. Then the film was soaked into the solution of GASCN and pure MeOAc for 3 s.) Ultraviolet-visible-near infrared spectra were recorded on a Perkin Elmer model Lambda 750. The PL spectra of QD solids were collected by a FluoroMax-4 spectrofluorometer (HORIBA Scientific). The TRPL results were acquired by a Fluo-time 300 (PicoQuant) system, and the samples were excited by a 405 nm laser. *C–V* measurements were performed using a precision impedance analyzer 6500B series. UPS measurements were performed using an Omicron Nanotechnology system with a base pressure of 2×10^{-10} Torr. The device cross-section was characterized by SEM on a Zeiss Supra 55 field in high vacuum mode at accelerating voltage of 15 kV. EIS measurements were carried out through a Zahner IM6 electrochemical workstation.

Acknowledgements

This work was supported by the National Natural Science Foundation of China (Nos. 92163114, 22161142003, 52002260, 62022081, and 61974099), the Natural Science Foundation of Jiangsu Province of China (No. BK20200872), the State Key Laboratory of applied optics (No. SKLAO2020001A03), and Postdoctoral Science Foundation of China (No. 2021M702415). This work is also supported by Suzhou Key Laboratory of Functional Nano & Soft Materials, Collaborative Innovation Center of Suzhou Nano Science & Technology, the 111 Project,

and Joint International Research Laboratory of Carbon-Based Functional Materials and Devices. K. W. acknowledges the funding support from National Key Research and Development Program (No. 2017YFE0120400) and National Natural Science Foundation of China (No. 61875082).

Electronic Supplementary Material: Supplementary material (Absorbance, PL, TEM, UPS, SEM, SCLC, device performance, and EIS parameters) is available in the online version of this article at https://doi.org/10.1007/s12274-022-4195-8.

References

[1] Carey, G. H.; Abdelhady, A. L.; Ning, Z. J.; Thon, S. M.; Bakr, O. M.; Sargent, E. H. Colloidal quantum dot solar cells. *Chem. Rev.* **2015**, *115*, 12732–12763.

[2] Liu, Y.; Shi, G. Z.; Liu, Z. K.; Ma, W. L. Toward printable solar cells based on PbX colloidal quantum dot inks. *Nanoscale Horiz.* **2021**, *6*, 8–23.

[3] Voznyy, O.; Sutherland, B. R.; Ip, A. H.; Zhitomirsky, D.; Sargent, E. H. Engineering charge transport by heterostructuring solution-processed semiconductors. *Nat. Rev. Mater.* **2017**, *2*, 17026.

[4] Lee, H.; Song, H. J.; Shim, M.; Lee, C. Towards the commercialization of colloidal quantum dot solar cells: Perspectives on device structures and manufacturing. *Energy Environ. Sci.* **2020**, *13*, 404–431.

[5] Gan, J.; Yu, M.; Hoye, R. L. Z.; Musselman, K. P.; Li, Y.; Liu, X.; Zheng, Y.; Zu, X.; Li, S.; MacManus-Driscoll, J. L. et al. Defects, photophysics and passivation in Pb-based colloidal quantum dot photovoltaics. *Mater. Today Nano* **2021**, *13*, 100101.

[6] McDonald, S. A.; Konstantatos, G.; Zhang, S. G.; Cyr, P. W.; Klem, E. J. D.; Levina, L.; Sargent, E. H. Solution-processed PbS quantum dot infrared photodetectors and photovoltaics. *Nat. Mater.* **2005**, *4*, 138–142.

[7] Luther, J. M.; Gao, J. B.; Lloyd, M. T.; Semonin, O. E.; Beard, M. C.; Nozik, A. J. Stability assessment on a 3% bilayer PbS/ZnO quantum dot heterojunction solar cell. *Adv. Mater.* **2010**, *22*, 3704–3707.

[8] Gao, J. B.; Perkins, C. L.; Luther, J. M.; Hanna, M. C.; Chen, H. Y.; Semonin, O. E.; Nozik, A. J.; Ellingson, R. J.; Beard, M. C. N-type transition metal oxide as a hole extraction layer in PbS quantum dot solar cells. *Nano Lett.* **2011**, *11*, 3263–3266.

[9] Tang, J.; Kemp, K. W.; Hoogland, S.; Jeong, K. S.; Liu, H.; Levina, L.; Furukawa, M.; Wang, X. H.; Debnath, R.; Cha, D. et al. Colloidal-quantum-dot photovoltaics using atomic-ligand passivation. *Nat. Mater.* **2011**, *10*, 765–771.

[10] Ip, A. H.; Thon, S. M.; Hoogland, S.; Voznyy, O.; Zhitomirsky, D.; Debnath, R.; Levina, L.; Rollny, L. R.; Carey, G. H.; Fischer, A. et al. Hybrid passivated colloidal quantum dot solids. *Nat. Nanotechnol.* **2012**, *7*, 577–582.

[11] Chuang, C. H. M.; Brown, P. R.; Bulovic, V.; Bawendi, M. G. Improved performance and stability in quantum dot solar cells through band alignment engineering. *Nat. Mater.* **2014**, *13*, 796–801.

[12] Lan, X. Z.; Voznyy, O.; Kiani, A.; De Arquer, F. P. G.; Abbas, A. S.; Kim, G. H.; Liu, M. X.; Yang, Z. Y.; Walters, G.; Xu, J. X. et al. Passivation using molecular halides increases quantum dot solar cell performance. *Adv. Mater.* **2016**, *28*, 299–304.

[13] Liu, M. X.; Voznyy, O.; Sabatini, R.; De Arquer, F. P. G.; Munir, R.; Balawi, A. H.; Lan, X. Z.; Fan, F. J.; Walters, G.; Kirmani, A. R. et al. Hybrid organic-inorganic inks flatten the energy landscape in colloidal quantum dot solids. *Nat. Mater.* **2017**, *16*, 258–263.

[14] Xu, J. X.; Voznyy, O.; Liu, M. X.; Kirmani, A. R.; Walters, G.; Munir, R.; Abdelsamie, M.; Proppe, A. H.; Sarkar, A.; De Arquer, F. P. G. et al. 2D matrix engineering for homogeneous quantum dot coupling in photovoltaic solids. *Nat. Nanotechnol.* **2018**, *13*, 456–462.

[15] Liu, M. X.; Chen, Y. L.; Tan, C. S.; Quintero-Bermudez, R.; Proppe, A. H.; Munir, R.; Tan, H. R.; Voznyy, O.; Scheffel, B.; Walters, G. et al. Lattice anchoring stabilizes solution-processed semiconductors. *Nature* **2019**, *570*, 96–101.

[16] Choi, M. J.; De Arquer, F. P. G.; Proppe, A. H.; Seifitokaldani, A.; Choi, J.; Kim, J.; Baek, S. W.; Liu, M. X.; Sun, B.; Biondi, M. et al. Cascade surface modification of colloidal quantum dot inks enables efficient bulk homojunction photovoltaics. *Nat. Commun.* **2020**, *11*, 103.

[17] Sun, B.; Johnston, A.; Xu, C.; Wei, M. Y.; Huang, Z. R.; Jiang, Z.; Zhou, H.; Gao, Y. J.; Dong, Y. T.; Ouellette, O. et al. Monolayer perovskite bridges enable strong quantum dot coupling for efficient solar cells. *Joule* **2020**, *4*, 1542–1556.

[18] Kim, H. I.; Baek, S. W.; Cheon, H. J.; Ryu, S. U.; Lee, S.; Choi, M. J.; Choi, K.; Biondi, M.; Hoogland, S.; De Arquer, F. P. G. et al. A tuned alternating D-A copolymer hole-transport layer enables colloidal quantum dot solar cells with superior fill factor and efficiency. *Adv. Mater.* **2020**, *32*, 2004985.

[19] Hu, L.; Zhao, Q.; Huang, S. J.; Zheng, J. H.; Guan, X. W.; Patterson, R.; Kim, J.; Shi, L.; Lin, C. H.; Lei, Q. et al. Flexible and efficient perovskite quantum dot solar cells via hybrid interfacial architecture. *Nat. Commun.* **2021**, *12*, 466.

[20] Fakharuddin, A.; Schmidt-Mende, L.; Garcia-Belmonte, G.; Jose, R.; Mora-Sero, I. Interfaces in perovskite solar cells. *Adv. Energy Mater.* **2017**, *7*, 1700623.

[21] Correa-Baena, J. P.; Tress, W.; Domanski, K.; Anaraki, E. H.; Turren-Cruz, S. H.; Roose, B.; Boix, P. P.; Grätzel, M.; Saliba, M.; Abate, A. et al. Identifying and suppressing interfacial recombination to achieve high open-circuit voltage in perovskite solar cells. *Energy Environ. Sci.* **2017**, *10*, 1207–1212.

[22] Stolterfoht, M.; Caprioglio, P.; Wolff, C. M.; Márquez, J. A.; Nordmann, J.; Zhang, S. S.; Rothhardt, D.; Hörmann, U.; Amir, Y.; Redinger, A. et al. The impact of energy alignment and interfacial recombination on the internal and external open-circuit voltage of perovskite solar cells. *Energy Environ. Sci.* **2019**, *12*, 2778–2788.

[23] Lu, K. Y.; Wang, Y. J.; Liu, Z. K.; Han, L.; Shi, G. Z.; Fang, H. H.; Chen, J.; Ye, X. C.; Chen, S.; Yang, F. et al. High-efficiency PbS quantum-dot solar cells with greatly simplified fabrication processing via "solvent-curing". *Adv. Mater.* **2018**, *30*, 1707572.

[24] Wang, Y. J.; Liu, Z. K.; Huo, N. J.; Li, F.; Gu, M. F.; Ling, X. F.; Zhang, Y. N.; Lu, K. Y.; Han, L.; Fang, H. H. et al. Room-temperature direct synthesis of semi-conductive PbS nanocrystal inks for optoelectronic applications. *Nat. Commun.* **2019**, *10*, 5136.

[25] Shi, G. Z.; Wang, H. B.; Zhang, Y. H.; Cheng, C.; Zhai, T. S.; Chen, B. T.; Liu, X. Y.; Jono, R.; Mao, X. N.; Liu, Y. et al. The effect of water on colloidal quantum dot solar cells. *Nat. Commun.* **2021**, *12*, 4381.

[26] Hu, L.; Lei, Q.; Guan, X. W.; Patterson, R.; Yuan, J. Y.; Lin, C. H.; Kim, J.; Geng, X.; Younis, A.; Wu, X. X. et al. Optimizing surface chemistry of PbS colloidal quantum dot for highly efficient and stable solar cells via chemical binding. *Adv. Sci.* **2021**, *8*, 2003138.

[27] Ding, C.; Liu, F.; Zhang, Y. H.; Hayase, S.; Masuda, T.; Wang, R. X.; Zhou, Y.; Yao, Y. F.; Zou, Z. G.; Shen, Q. Passivation strategy of reducing both electron and hole trap states for achieving high-efficiency PbS quantum-dot solar cells with power conversion efficiency over 12%. *ACS Energy Lett.* **2020**, *5*, 3224–3236.

[28] Wang, R. L.; Shang, Y. Q.; Kanjanaboos, P.; Zhou, W. J.; Ning, Z. J.; Sargent, E. H. Colloidal quantum dot ligand engineering for high performance solar cells. *Energy Environ. Sci.* **2016**, *9*, 1130–1143.

[29] Chen, J. X.; Zheng, S. Y.; Jia, D. L.; Liu, W. L.; Andruszkiewicz, A.; Qin, C. C.; Yu, M.; Liu, J. H.; Johansson, E. M. J.; Zhang, X. L. Regulating thiol ligands of p-type colloidal quantum dots for efficient infrared solar cells. *ACS Energy Lett.* **2021**, *6*, 1970–1979.

[30] Aqoma, H.; Mubarok, M. A.; Lee, W.; Hadmojo, W. T.; Park, C.; Ahn, T. K.; Ryu, D. Y.; Jang, S. Y. Improved processability and efficiency of colloidal quantum dot solar cells based on organic hole transport layers. *Adv. Energy Mater.* **2018**, *8*, 1800572.

[31] Xue, Y.; Yang, F.; Yuan, J. Y.; Zhang, Y. N.; Gu, M. F.; Xu, Y. L.; Ling, X. F.; Wang, Y.; Li, F. C.; Zhai, T. S. et al. Toward scalable PbS quantum dot solar cells using a tailored polymeric hole conductor. *ACS Energy Lett.* **2019**, *4*, 2850–2858.

[32] Mubarok, M. A.; Wibowo, F. T. A.; Aqoma, H.; Krishna, N. V.; Lee, W.; Ryu, D. Y.; Cho, S.; Jung, I. H.; Jang, S. Y. PbS-based quantum dot solar cells with engineered π-conjugated polymers achieve 13% efficiency. *ACS Energy Lett.* **2020**, *5*, 3452–3460.

[33] Mubarok, M. A.; Aqoma, H.; Wibowo, F. T. A.; Lee, W.; Kim, H. M.; Ryu, D. Y.; Jeon, J. W.; Jang, S. Y. Molecular engineering in hole transport π-conjugated polymers to enable high efficiency colloidal quantum dot solar cells. *Adv. Energy Mater.* **2020**, *10*, 1902933.

[34] Baek, S. W.; Jun, S.; Kim, B.; Proppe, A. H.; Ouellette, O.; Voznyy, O.; Kim, C.; Kim, J.; Walters, G.; Song, J. H. et al. Efficient hybrid colloidal quantum dot/organic solar cells mediated by near-infrared sensitizing small molecules. *Nat. Energy* **2019**, *4*, 969–976.

[35] Zhang, Y. N.; Kan, Y. Y.; Gao, K.; Gu, M. F.; Shi, Y.; Zhang, X. L.; Xue, Y.; Zhang, X. N.; Liu, Z. K.; Zhang, Y. et al. Hybrid quantum dot/organic heterojunction: A route to improve open-circuit voltage in PbS colloidal quantum dot solar cells. *ACS Energy Lett.* **2020**, *5*, 2335–2342.

[36] Baek, S. W.; Molet, P.; Choi, M. J.; Biondi, M.; Ouellette, O.; Fan, J.; Hoogland, S.; de Arquer, F. P. G.; Mihi, A.; Sargent, E. H. Nanostructured back reflectors for efficient colloidal quantum-dot infrared optoelectronics. *Adv. Mater.* **2019**, *31*, 1901745.

[37] Gao, F.; Ren, S. Q.; Wang, J. P. The renaissance of hybrid solar cells: Progresses, challenges, and perspectives. *Energy Environ. Sci.* **2013**, *6*, 2020–2040.

[38] Liu, Z. K.; Yuan, J. Y.; Hawks, S. A.; Shi, G. Z.; Lee, S. T.; Ma, W. L. Photovoltaic devices based on colloidal PbX quantum dots: Progress and prospects. *Sol. RRL* **2017**, *1*, 1600021.

[39] Swarnkar, A.; Marshall, A. R.; Sanehira, E. M.; Chernomordik, B. D.; Moore, D. T.; Christians, J. A.; Chakrabarti, T.; Luther, J. M. Quantum dot-induced phase stabilization of α-$CsPbI_3$ perovskite for high-efficiency photovoltaics. *Science* **2016**, *354*, 92–95.

[40] Kovalenko, M. V.; Protesescu, L.; Bodnarchuk, M. I. Properties and potential optoelectronic applications of lead halide perovskite nanocrystals. *Science* **2017**, *358*, 745–750.

[41] Gan, J. T.; He, J. X.; Hoye, R. L. Z.; Mavlonov, A.; Raziq, F.; MacManus-Driscoll, J. L.; Wu, X. Q.; Li, S.; Zu, X. T.; Zhan, Y. Q. et al. A-$CsPbI_3$ colloidal quantum dots: Synthesis, photodynamics, and photovoltaic applications. *ACS Energy Lett.* **2019**, *4*, 1308–1320.

[42] Yuan, J. Y.; Hazarika, A.; Zhao, Q.; Ling, X. F.; Moot, T.; Ma, W. L.; Luther, J. M. Metal halide perovskites in quantum dot solar cells: Progress and prospects. *Joule* **2020**, *4*, 1160–1185.

[43] Chen, J. X.; Jia, D. L.; Johansson, E. M. J.; Hagfeldt, A.; Zhang, X. L. Emerging perovskite quantum dot solar cells: Feasible approaches to boost performance. *Energy Environ. Sci.* **2021**, *14*, 224–261.

[44] Duan, L. P.; Hu, L.; Guan, X. W.; Lin, C. H.; Chu, D. W.; Huang, S. J.; Liu, X. G.; Yuan, J. Y.; Wu, T. Quantum dots for photovoltaics: A tale of two materials. *Adv. Energy Mater.* **2021**, *11*, 2100354.

[45] Akkerman, Q. A.; Rainò, G.; Kovalenko, M. V.; Manna, L. Genesis, challenges and opportunities for colloidal lead halide perovskite nanocrystals. *Nat. Mater.* **2018**, *17*, 394–405.

[46] Lanigan-Atkins, T.; He, X.; Krogstad, M. J.; Pajerowski, D. M.; Abernathy, D. L.; Xu, G. N. M. N.; Xu, Z. J.; Chung, D. Y.; Kanatzidis, M. G.; Rosenkranz, S. et al. Two-dimensional overdamped fluctuations of the soft perovskite lattice in $CsPbBr_3$. *Nat. Mater.* **2021**, *20*, 977–983.

[47] Wang, Y. J.; Lu, K. Y.; Han, L.; Liu, Z. K.; Shi, G. Z.; Fang, H. H.; Chen, S.; Wu, T.; Yang, F.; Gu, M. F. et al. *In situ* passivation for efficient PbS quantum dot solar cells by precursor engineering. *Adv. Mater.* **2018**, *30*, 1704871.

[48] Yuan, J. Y.; Ling, X. F.; Yang, D.; Li, F. C.; Zhou, S. J.; Shi, J. W.; Qian, Y. L.; Hu, J. X.; Sun, Y. S.; Yang, Y. G. et al. Band-aligned polymeric hole transport materials for extremely low energy loss α-$CsPbI_3$ perovskite nanocrystal solar cells. *Joule* **2018**, *2*, 2450–2463.

[49] Wheeler, L. M.; Sanehira, E. M.; Marshall, A. R.; Schulz, P.; Suri, M.; Anderson, N. C.; Christians, J. A.; Nordlund, D.; Sokaras, D.; Kroll, T. et al. Targeted ligand-exchange chemistry on cesium lead halide perovskite quantum dots for high-efficiency photovoltaics. *J. Am. Chem. Soc.* **2018**, *140*, 10504–10513.

[50] Ling, X. F.; Yuan, J. Y.; Zhang, X. L.; Qian, Y. L.; Zakeeruddin, S. M.; Larson, B. W.; Zhao, Q.; Shi, J. W.; Yang, J. C.; Ji, K. et al. Guanidinium-assisted surface matrix engineering for highly efficient perovskite quantum dot photovoltaics. *Adv. Mater.* **2020**, *32*, 2001906.

[51] Lu, K. Y.; Wang, Y. J.; Yuan, J. Y.; Cui, Z. Q.; Shi, G. Z.; Shi, S. H.; Han, L.; Chen, S.; Zhang, Y. N.; Ling, X. F. et al. Efficient PbS quantum dot solar cells employing a conventional structure. *J. Mater. Chem. A* **2017**, *5*, 23960–23966.

[52] Wang, Z.; Gan, J. T.; Liu, X. D.; Shi, H. B.; Wei, Q.; Zeng, Q. G.; Qiao, L.; Zheng, Y. H. Over 1 μm electron-hole diffusion lengths in $CsPbI_2Br$ for high efficient solar cells. *J. Power Sources* **2020**, *454*, 227913.

[53] Li, F.; Liu, Y.; Shi, G. Z.; Chen, W.; Guo, R. J.; Liu, D.; Zhang, Y. H.; Wang, Y. J.; Meng, X.; Zhang, X. L. et al. Matrix manipulation of directly-synthesized PbS quantum dot inks enabled by coordination engineering. *Adv. Funct. Mater.* **2021**, *31*, 2104457.